
Article:
Aldean, I., Sun, S.-K., Wilkins, M.C.D. et al. (6 more authors) (2022) Synthesis and characterisation of Ce-doped zirconolite Ca0.80Ce0.20ZrTi1.60M0.40O7 (M = Fe, Al) formed by reactive spark plasma sintering (RSPS). MRS Advances, 7. pp. 75-80. ISSN 2731-5894

https://doi.org/10.1557/s43580-022-00221-6

MRS Advances
https://doi.org/10.1557/s43580-022-00221-6

ORIGINAL PAPER

Synthesis and characterisation of Ce-doped zirconolite $Ca_{0.80}Ce_{0.20}ZrTi_{1.60}M_{0.40}O_7$ (M = Fe, Al) formed by reactive spark plasma sintering (RSPS)

Ismail Aldean[1] · Shi-Kuan Sun[2] · Malin C. Dixon Wilkins[1] · Laura J. Gardner[1] · Amber R. Mason[1] · Martin C. Stennett[1] · Claire L. Corkhill[1] · Neil C. Hyatt[1] · Lewis R. Blackburn[1]

Received: 29 November 2021 / Accepted: 27 January 2022

Abstract
Reactive spark plasma sintering has been utilised as a high-throughput processing route for the synthesis of two simulant zirconolite wasteform materials, targeting $Ca_{0.80}Ce_{0.20}ZrTi_{1.60}M_{0.40}O_7$ (M = Fe^{3+} and Al^{3+}). Materials were processed under 15 MPa uniaxial pressure, with heating/cooling rates of 100 °C/min to 1320 °C, maintained under vacuum. Despite moderate yield (> 80 wt%) of zirconolite-2M, a considerable Ce-rich perovskite phase was formed in both formulations, attributed to complete reduction of the Ce inventory to Ce^{3+}, as determined by Ce L_3-edge XANES analysis. The composition charge balanced with Al^{3+} was favoured on the basis of lower accompanying perovskite fraction.

Introduction

A strategy combining reuse, immobilisation and disposal has been proposed as a long-term solution for at least some portion of the United Kingdom civil PuO_2 inventory, which is forecast to reach ~ 140 teHM (tonnes equivalent heavy metal) once domestic reprocessing operations cease [1]. Prior to placement alongside the existing HLW inventory in a geological disposal facility (GDF) Pu must first be immobilised at the atomic scale in a high-durability matrix, to confer passive safety and improve handling properties. Fundamentally, the primary driver for immobilisation is to prevent Pu migration into the near-field environment over geological timescales such that the overall activity of the waste package at the time of failure is similar to the U ore from which it was derived. On the basis of high chemical durability and radiation stability, crystalline titanate materials (including hollandite, pyrochlore, perovskite, brannerite and zirconolite) are suitable phases for the sequestration of partitioned actinides (Pu, Am, U) and fission products (Cs, Sr) present in many nuclear waste streams. The zirconolite phase (ideally $CaZrTi_2O_7$) is considered to be the most suitable matrix for the immobilisation of Pu [2]. The zirconolite-2M parent structure is a derivation of an anion-deficient fluorite superstructure, composed of layered TiO_6/TiO_5 polyhedra, arranged in a hexagonal-tungsten-bronze (HTB)-type motif interspaced with layers of CaO_8/ZrO_7 polyhedra, with the overall structure crystallising in the space group C2/c ($Z = 8$, $\rho = 4.47$ g/cm^3) [3]. The chemical flexibility of the zirconolite phase is one of the primary drivers towards its use as a wasteform as there are five distinct cation receptor sites that are capable of accommodating actinides, neutron poisoning additives (typically Gd^{3+} and Hf^{4+} on the basis of compatible oxidation state and ionic radius) and charge compensating species. Typically, larger waste cations such as $Pu^{3+/4+}$ are most suitably accommodated within the Ca^{2+} site on the basis of ionic radii, with lower valence charge balancing cations (typically Fe^{3+} or Al^{3+}) co-substituted in an appropriate molar ratio within the Ti^{4+} sites. Substitution of tetravalent cations on the Zr^{4+} site produces a transformation to zirconolite-4M, a superstructure composed of alternating layers of zirconolite-2M and pyrochlore-type modules, resulting in a doubling of the unit cell along the c-axis [4–6]. Substitution on the Ca^{2+} site has been observed, in some instances, to promote the formation of the trigonal variant zirconolite-3T; a number of such solid solutions have been reported in the literature [4, 7–9]. In the present study,

✉ Lewis R. Blackburn
lewis.blackburn@sheffield.ac.uk

1 Immobilisation Science Laboratory, Department of Materials Science and Engineering, University of Sheffield, Sir Robert Hadfield Building, Mappin Street, Sheffield S1 3JD, UK

2 School of Material Science and Energy Engineering, Foshan University, Foshan 528000, China

Published online: 07 February 2022

with Ce utilised as a surrogate for Pu, reactive spark plasma sintering (RSPS) has been deployed as a high-throughput synthesis route to fabricate zirconolite ceramics with the formulation $Ca_{0.80}Ce_{0.20}ZrTi_{1.60}M_{0.40}O_7$ where $M = Fe^{3+}$ or Al^{3+}. RSPS is a potentially attractive route for the ceramic immobilisation of actinides, given the throughput that can be achieved. A detailed review discussing the application of spark plasma sintering in the context of phosphate wasteform development was recently published [10]. The simultaneous synthesis and consolidation of ceramic materials via RSPS are achieved by rapid DC current pulsing through a compressed powder compact, maintained under uniaxial pressure. This allows the production of monoliths of near theoretical density, even in short processing times, due to heating/cooling rates typically of the order 100 °C/min [11]. The process has previously been demonstrated as suitable for the effective immobilisation of ^{129}I in lead vanadophosphate iodoapatite $Pb_{10}(VO_4)_{4.8}(PO_4)O_{1.2}I_2$) [12], Cs in hollandite (nominally $BaAl_2Ti_6O_{16}$) [13], and more recently Ce in zirconolite [9].

Experimental methodology

Materials synthesis

Oxide powders $CaTiO_3$ (99.9%, Sigma Aldrich), ZrO_2 (99.9%, Sigma Aldrich), CeO_2 (99.9%, Acros Organics), TiO_2 (anatase, 99.9%, Sigma Aldrich), Al_2O_3 (99.9%, Sigma Aldrich), and Fe_2O_3 (99.9%, Sigma Aldrich) were calcined at 800 °C for 12 h, prior to addition to a ZrO_2-lined milling vessel, in stoichiometric ratios according to the formulations $Ca_{0.80}Ce_{0.20}ZrTi_{1.60}Al_{0.40}O_7$ and $Ca_{0.80}Ce_{0.20}ZrTi_{1.60}Fe_{0.40}O_7$. The mixtures were homogenised using a Fritsch P7 planetary ball mill, with ZrO_2 milling media and isopropanol, at 400 rpm for a total of 20 min. Samples were recovered and dried at 80 °C to evaporate excess solvent. Approximately 5 g of each batch was measured and transferred to a 20 mm graphite die, with graphite foil spacers to promote uniform current flow, and compressed under 3 t for approximately 5 min to form loosely bound green bodies. The die was then loaded into a HP-D 1050 SPS system (FCT Systeme GmBH) and ramped at 100 °C/min to 1320 °C, with a constant uniaxial pressure of 15 MPa maintained throughout. A simplified illustration of this configuration is provided in Fig. 1, alongside a photograph of a typical product.

Materials characterisation

Post-sintering, pellets were sectioned and prepared for powder X-ray diffraction (XRD) using a Bruker D2 Phaser diffractometer, fitted with Lynxeye position sensitive detector utilising Cu-Kα radiation ($\lambda = 1.5418$ Å, Ni filter). Data were collected in the range $10° \leq 2\theta \leq 80°$. Rietveld analysis of powder XRD data was achieved using the Bruker TOPAS package [14]. The true density of each composition was determined by He-gas pycnometry, with material in the powder form. Density measurements were taken using an AccuPyc 1340 II pycnometer, with a total of 20 cycles performed for each specimen under

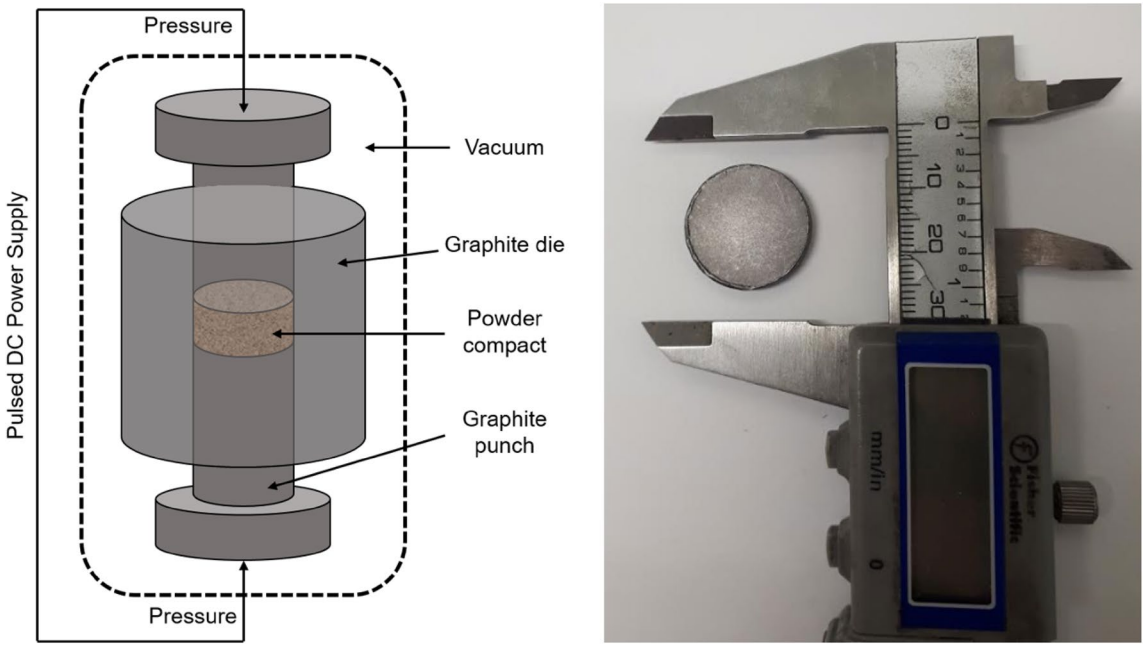

Fig. 1 Simplified illustration of RSPS configuration (left) and photograph of a typical ceramic product (right)

a fill pressure of 12.5 psi. A representative portion of the microstructure was sectioned from the monoliths and prepared for analysis by scanning electron microscopy (SEM) using a Hitachi TM3030 operating at 15 kV accelerating voltage with a working distance of 8 mm. This was fitted with a Bruker Quantax Elemental Dispersive X-ray Spectrometer (EDS) for semi-quantitative compositional analysis. Samples were prepared for SEM–EDS by cold setting in epoxy resin, prior to polishing to a 1 µm optical finish and coating with a conductive amorphous carbon layer to reduce surface-charging effects. Ce L_3-edge X-ray absorption near edge spectroscopy (XANES) data were collected at room temperature at Beamline BL-27 at the Photon Factory (PF) accelerator light source (Tsukuba, Japan). The optical arrangement is composed of a double Si(111) monochromator, with slits used to reduce the beam footprint to 3 × 1 mm. Samples were prepared for XANES analysis by suspension of sufficient material to form one absorption length in an inert, low absorbance binder (polyethylene glycol, PEG) in pressed 13 mm discs. Spectra were collected alongside a number of reference compounds of known Ce oxidation state and analysed using the Athena component of the Demeter software package [15].

Results and discussion

Analysis of powder XRD data (Fig. 2) revealed, for both Al^{3+} and Fe^{3+}-doped compositions, intense reflections consistent with the zirconolite-2M polytype occupying the dominant fraction of the phase assemblage. When targeting $Ca_{0.80}Ce_{0.20}ZrTi_{1.60}Al_{0.40}O_7$, a number of secondary reflections were identified, the most prominent of which was observed at $2\theta = 33.1°$, attributed to the (112) reflection of perovskite (nominally $CaTiO_3$). Additional weaker reflections consistent with Al_2O_3 and ZrO_2 were also distinguished. Quantitative phase analysis, derived from Rietveld profile fitting (Table 1) indicated that a yield of 83.5 ± 0.3 wt% zirconolite-2M was obtained. Unit cell parameters for the Al^{3+} formulation were in good agreement with previous observations, calculated to be: $a = 12.4903(5)$ Å, $b = 7.2487(3)$ Å, $c = 11.3762(4)$ Å, $\beta = 100.656(3)°$ and $V = 1012.22(7)$ Å^3. A greater relative proportion (14.5 ± 0.6 wt%) of perovskite was observed for the Fe^{3+} formulation demonstrating that, under the given processing conditions, Al^{3+} performed as a more effective charge compensation cation relative to Fe^{3+}. Rietveld refinement produced unit cell parameters for the Fe^{3+}-doped zirconolite-2M phase that were largely consistent with the Al^{3+} composition: $a = 12.4764(5)$ Å, $b = 7.2634(3)$ Å, $c = 11.4745(4)$ Å,

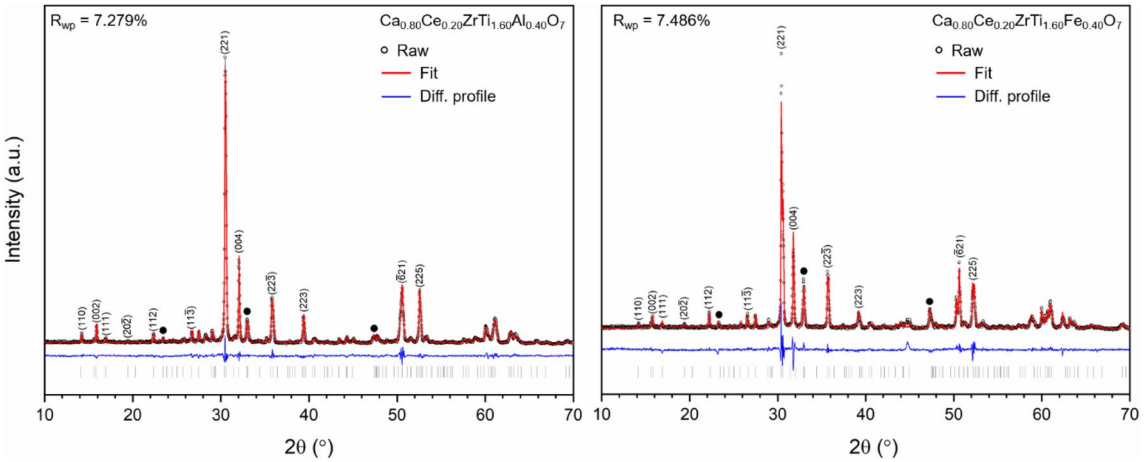

Fig. 2 Rietveld analysis of powder diffraction data for $Ca_{0.80}Ce_{0.20}ZrTi_{1.60}Al_{0.40}O_7$ (left) and $Ca_{0.80}Ce_{0.20}ZrTi_{1.60}Fe_{0.40}O_7$ (right) formulations (red line, calculated patterns; black circles, observed patterns; blue line, difference profile). Vertical tick marks indicate theoretical position of zirconolite-2M reflections. Observed zirconolite-2M reflections are labelled with (*hkl*) values. Perovskite reflections are labelled with closed circles (●)

Table 1 Quantitative phase output from the Rietveld analysis of powder XRD data

Composition	Phase Assemblage (wt%)					R_{wp} (%)
	Zirconolite-2M	Perovskite	ZrO_2	Fe_2O_3	Al_2O_3	
$Ca_{0.80}Ce_{0.20}ZrTi_{1.60}Al_{0.40}O_7$	83.5 ± 0.3	9.9 ± 0.2	3.6 ± 0.2	–	3.0 ± 0.2	7.279
$Ca_{0.80}Ce_{0.20}ZrTi_{1.60}Fe_{0.40}O_7$	82.2 ± 0.3	14.5 ± 0.6	–	3.3 ± 0.4	–	7.486

$\beta = 100.368(2)°$ and $V = 1022.85(7)$ Å^3, yet with a notable increase in unit cell volume. This may be attributed to the ionic radii of Al^{3+} (53 pm) and Fe^{3+} (63 pm) relative to Ti^{4+} (68 pm).

A representative portion of each microstructure is labelled and displayed in Fig. 3. It was clear that both specimens formed with a fine-grained, high-density microstructure. He-gas pycnometry determined the true density of the formed products to be 4.6071 ± 0.0038 and 4.7976 ± 0.0115 g/cm^3 for Al^{3+} and Fe^{3+} compositions, respectively. It was clear that when synthesising materials targeting both Al^{3+} and Fe^{3+} charge compensation, a moderately heterogeneous phase assemblage was formed, with apparent phase distributions consistent with quantitative phase analyses derived from the Rietveld fitting. Upon inspection of the materials batched as $Ca_{0.80}Ce_{0.20}ZrTi_{1.60}Al_{0.40}O_7$, clear islands of ZrO_2 and Al_2O_3 were present, with regions of fine-grained Ce-substituted $CaTiO_3$ clearly distinguished by complementary EDS phase analysis (not shown). Similar observations were made for the Fe^{3+}-substituted sample; it was also clear that the Ce-perovskite occupied a greater proportion of the microstructure, in agreement with the Rietveld analysis of powder diffraction data discussed above. EDS analysis of perovskite grains present in the material batched as $Ca_{0.80}Ce_{0.20}ZrTi_{1.60}Fe_{0.40}O_7$ demonstrated uptake of a significant portion of Ce (Fig. 4). It was clear in early studies on SYNROC (SYNthetic-ROCk) corrosion that perovskite was the least durable phase in the conventional SYNROC-C wasteform under dissolution conditions [16]. Therefore, partial sequestration of the Pu surrogate fraction within the

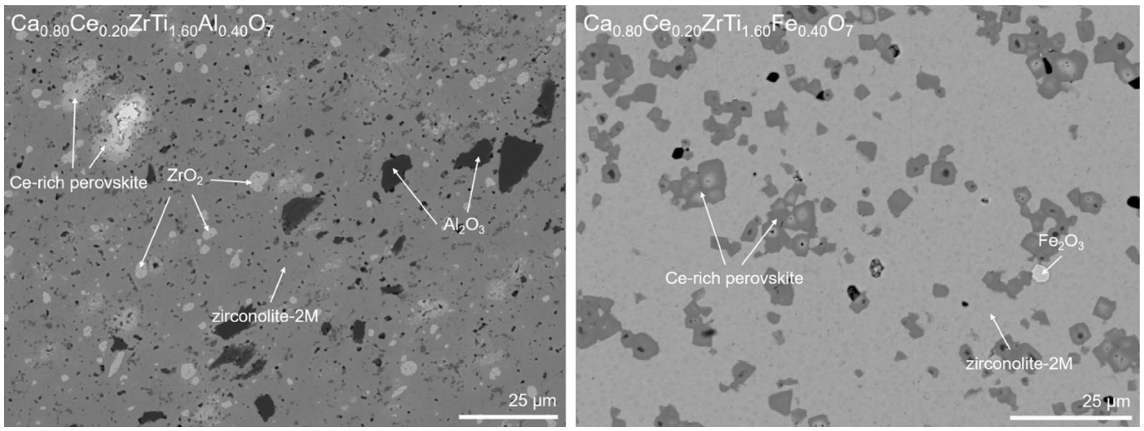

Fig. 3 Backscattered electron micrograph for representative sections of materials batched targeting the compositions $Ca_{0.80}Ce_{0.20}ZrTi_{1.60}Al_{0.40}O_7$ (left) and $Ca_{0.80}Ce_{0.20}ZrTi_{1.60}Fe_{0.40}O_7$ (right)

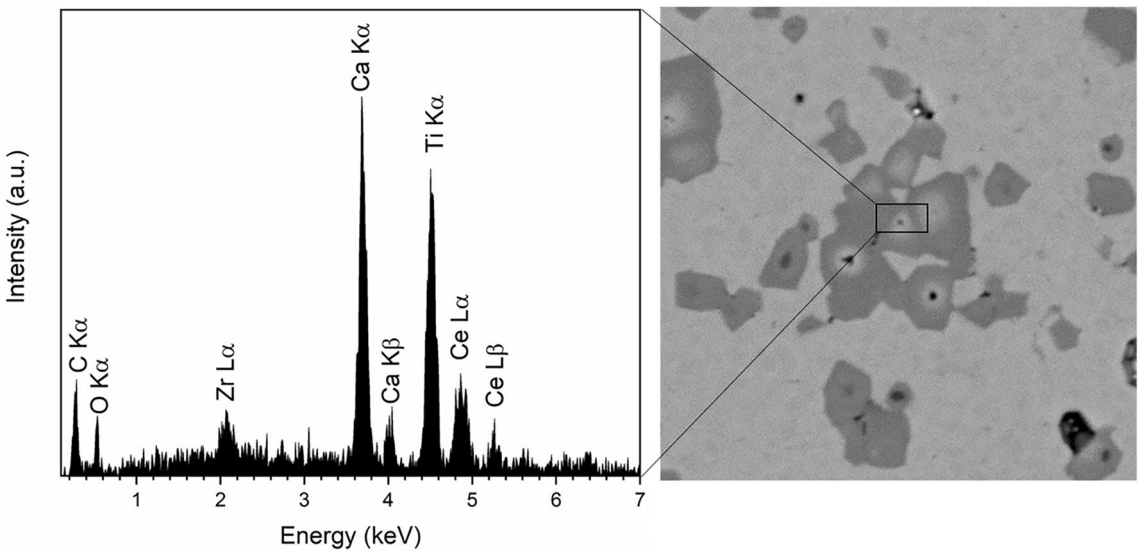

Fig. 4 EDS analysis of a perovskite cluster present in the material targeting $Ca_{0.80}Ce_{0.20}ZrTi_{1.60}Fe_{0.40}O_7$, presenting a signal corresponding to the Ce Lα emission line

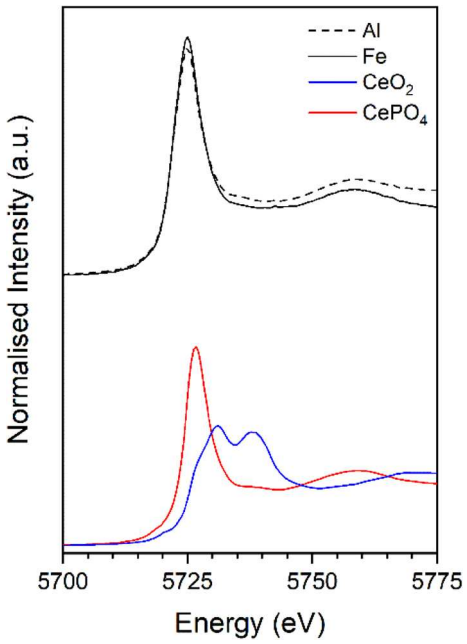

Fig. 5 Above: Ce L_3-edge XANES spectra of materials targeting $Ca_{0.80}Ce_{0.20}ZrTi_{1.60}Al_{0.40}O_7$ (labelled as Al) and $Ca_{0.80}Ce_{0.20}ZrTi_{1.60}Fe_{0.40}O_7$ (labelled as Fe). Below: spectra of the CeO_2 and $CePO_4$ reference compounds

perovskite phase would be expected to significantly decrease the overall durability of such wasteforms, given the lower chemical durability of this phase relative to the targeted zirconolite matrix. In a recent publication, we demonstrated that, when carefully dissolved under aggressive leaching media, the extent to which a Ce surrogate inventory was extracted into solution could be decreased by a factor of 100 through altering the batch formulation to precluding the formation of an ancillary perovskite phase [17].

In order to determine the prevalent Ce oxidation state, Ce L_3-XANES data were collected alongside the reference compounds $Ce^{4+}O_2$ and $Ce^{3+}PO_4$ (Fig. 5). Both RSPS samples exhibited a single intense asymmetric white line feature consistent with uniform Ce^{3+} speciation when compared qualitatively with the $CePO_4$ reference compound (in which Ce^{3+} is ninefold coordinated to oxygen). No features consistent with Ce^{4+} were presented, confirming that the reducing environment imposed by the graphite SPS die was sufficient to completely reduce the available Ce^{4+} inventory to Ce^{3+}, and subsequently, promote Ce substitution within the perovskite phase. Moreover, linear combination analysis of Ce L_3-XANES data using the spectra of reference compounds was consistent with 100% Ce^{3+} speciation in the ceramic formulations. These data are consistent with previous studies, wherein sintering of Ce-substituted zirconolite under reducing conditions resulted in the formation of a significant perovskite fraction [18].

Conclusions

Reactive spark plasma sintering has been utilised to synthesise two synthetic zirconolite wasteform materials, targeting $Ca_{0.80}Ce_{0.20}ZrTi_{1.60}Al_{0.40}O_7$ and $Ca_{0.80}Ce_{0.20}ZrTi_{1.60}Al_{0.40}O_7$, with Ce included as a Pu surrogate. Despite the rapid (< 1 h total processing time per sample) formation of high-density ceramic monoliths, a significant portion of the phase assemblage was composed of Ce-rich perovskite, the stability of which was attributed to the complete reduction of the available Ce inventory to Ce^{3+}. These data form a useful contribution towards ongoing efforts to design suitable wasteform compositions for Pu immobilisation and optimisation of processing routes for these materials.

Acknowledgments We acknowledge financial support from the Nuclear Decommissioning Authority (NDA) and EPSRC under Grant Numbers EP/S01019X/1, EP/N017870/1 and EP/R511754/1. This research utilised the HADES/ MIDAS facility at the University of Sheffield established with financial support from EPSRC and BEIS, under grant EP/T011424/1 [19]. Collection of the Ce L_3-edge XAS data was performed under the approval of the Photon Factory Advisory Committee (Proposal No. 2019G586); the support of Yoshihiro Okamoto (Japanese Atomic Energy Agency) and Noriko Usami (The High Energy Accelerator Research Organisation—Kō Enerugī Kasokuki Kenkyū Kikō) during the experiment is gratefully acknowledged.

Data availability The data that support the findings of this study are available from the corresponding author upon reasonable request.

Declarations

Conflict of interest The authors declare that they have no known competing financial interests or personal relationships that could have appeared to influence the work reported in this paper.

References

1. N.C. Hyatt, Safe management of the UK separated plutonium inventory: a challenge of materials degradation. NPJ Mater. Degrad. **4**, 28 (2020)
2. L.R. Blackburn, N.C. Hyatt, Actinide immobilisation in dedicated wasteforms: an alternative pathway for the long-term management of existing actinide stockpiles, in *Encyclopedia*

of Nuclear Energy, 1st edn., ed. by E. Greenspan (Elsevier, Amsterdam, 2021), pp. 650–662
3. L.R. Blackburn et al., Review of zirconolite crystal chemistry and aqueous durability. Adv. Appl. Ceram. **120**(2), 1–15 (2021)
4. E.R. Vance et al., Incorporation of uranium in zirconolite ($CaZrTi_2O_7$). J. Am. Ceram. Soc. **85**(7), 1853–1859 (2002)
5. B.D. Begg, R.A. Day, A. Brownscombe, Structural effect of Pu substitutions on the Zr-site in zirconolite. Mater. Res. Soc. Symp. Proc. **663**, 1–8 (2001)
6. L.R. Blackburn, S. Sun, L.J. Gardner, E.R. Maddrell, M.C. Stennett, N.C. Hyatt, A systematic investigation of the phase assemblage and microstructure of the zirconolite $CaZr_{1-x}Ce_xTi_2O_7$ system. J. Nucl. Mater. **535**, 152137 (2020)
7. M.-X. Zhong et al., Synthesis of $Ca_{1-x}Ce_xZrTi_{2-2x}Al_{2x}O_7$ zirconolite ceramics for plutonium disposition. J. Nucl. Mater. **556**, 153198 (2021)
8. M.R. Gilbert et al., Synthesis and characterisation of Pu-doped zirconolites: $(Ca_{1-x}Pu_x)Zr(Ti_{2-2x}Fe_{2x})O_7$, in *IOP Conf. Ser. Mater. Sci. Eng.*, vol. 9, no. 012007, 2010.
9. L.R. Blackburn et al., Synthesis and characterisation of $Ca_{1-x}Ce_xZrTi_{2-2x}Cr_{2x}O_7$: analogue zirconolite wasteform for the immobilisation of stockpiled UK plutonium. J. Eur. Ceram. Soc. **40**(15), 5909–5919 (2020)
10. A.I. Orlova, Crystalline phosphates for HLW immobilization—composition, structure, properties and production of ceramics. Spark plasma sintering as a promising sintering technology. J. Nucl. Mater. **559**, 153407 (2022)
11. M. Suarez *et al.*, Challenges and opportunities for spark plasma sintering: a key technology for a new generation of materials, in *Sintering Applications*, 2013.
12. L. Campayo et al., Relevance of the choice of spark plasma sintering parameters in obtaining a suitable microstructure for iodine-bearing apatite designed for the conditioning of I-129. J. Nucl. Mater. **457**, 63–71 (2015)
13. B.M. Clark, P. Tumurugoti, S.K. Sundaram, J.W. Amoroso, J.C. Marra, K.S. Brinkman, Microstructures of melt-processed and spark plasma sintered ceramic waste forms. Metall. Mater. Trans. E **1E**, 341–348 (2014)
14. A.A. Coelho, J. Evans, I. Evans, A. Kern, S. Parsons, The TOPAS symbolic computation system. Powder Diffr. **26**(S1), S22–S25 (2011)
15. B. Ravel, M. Newville, ATHENA, ARTEMIS, HEPHAESTUS: data analysis for X-ray absorption spectroscopy using IFEFFIT. J. Synchrotron Radiat. **12**, 537–541 (2005)
16. K.L. Smith, G.R. Lumpkin, M.G. Blackford, R.A. Day, K.P. Hart, The durability of synroc. J. Nucl. Mater. **190**, 287–294 (1992)
17. L.R. Blackburn et al., "Influence of accessory phases and surrogate type on accelerated leaching of zirconolite wasteforms. npj Mater. Degrad. **5**(24), 1–11 (2021)
18. B.M. Clark, S.K. Sundaram, S.T. Misture, Polymorphic transitions in cerium-substituted zirconolite ($CaZrTi_2O_7$). Sci. Rep. **7**(1), 2–10 (2017)
19. N.C. Hyatt, C.L. Corkhill, M.C. Stennett, R.J. Hand, L.J. Gardner, C.L. Thorpe, The HADES facility for high activity decommissioning engineering & science: part of the UK National Nuclear User Facility, in *IOP Conf. Series: Materials Science and Engineering*, 2020, vol. 818, pp. 1–8.